

# THERMAL MEASUREMENTS IN THE FRAMEWORK OF SPARC

J.A. Sobrino<sup>(1)</sup>, M. Romaguera<sup>(1)</sup>, G. Sòria<sup>(1)</sup>, M. M. Zaragoza<sup>(1)</sup>, M. Gómez<sup>(1)</sup>, J. Cuenca<sup>(1)</sup>, Y. Julien<sup>(1)</sup>, J.C. Jiménez-Muñoz<sup>(1)</sup>, Z. Su<sup>(2)</sup>, L. Jia<sup>(3)</sup>, A. Gieske<sup>(2)</sup>, W. Timmermans<sup>(2)</sup>, H. Van der Kwast<sup>(4)</sup>, A. Oliosio<sup>(5)</sup>, F. Nerry<sup>(6)</sup>, D. Sabol<sup>(7)</sup> and J. Moreno<sup>(8)</sup>

(1) Global Change Unit, Department of Thermodynamics, University of Valencia, Dr. Moliner 50, 46100 Burjassot, Spain, [sobrino@uv.es](mailto:sobrino@uv.es)

(2) International Institute for Geo-Information Science and Earth Observation (ITC), Enschede, The Netherlands

(3) Alterra, Wageningen University and Research Centre, Wageningen, The Netherlands

(4) University of Utrecht, Utrecht, The Netherlands

(5) INRA, Avignon, France

(6) TRIO/ULP, Strasbourg, France

(7) University of Washington, Seattle, U.S.A.

(8) University of Valencia, Valencia, Spain

## ABSTRACT

In this paper, a description of the thermal radiometric measurements carried out in the framework of the Spectra Barrax Campaign (SPARC) is presented. The purpose of these measurements is to retrieve biogeophysical parameters such as land surface emissivity and temperature to analyze the relationship of these parameters with fluorescence. The *in situ* data base was used to validate high and low resolution sensors such as Airborne Hyperspectral Scanner (AHS), Advanced Spaceborne Thermal Emission and Reflection Radiometer (ASTER), Spinning Enhanced Visible and Infrared Imager (SEVIRI) and Advanced Along-Track Scanning Radiometer (AATSR), and a synergistic study was firstly developed between SEVIRI and ASTER and secondly between AATSR and CHRIS/PROBA (Compact High Resolution Imaging Spectrometer/Project for On Board Autonomy). The thermal measurements were carried out basically using two multiband field radiometers (CIMEL CE 312-1 and 312-2) and several single band field radiometers (RAYTEK ST6, RAYTEK MID and EVEREST 3000.4ZLC), pointing at different targets (soil, vegetation, sky). Transects, angular and emissivity measurements were carried out and the results show the importance of thermal measurements to characterize the different surfaces over the test area.

## 1. REGION OF STUDY AND INSTRUMENTS

The measurements campaign was developed in the Barrax field site, located in the south of Spain approximately 20 km away from Albacete (39°3' N, 2°6' W, 700m elevation). Fig.1 shows the different test parcels analysed.

Radiometric measurements were carried out in the thermal infrared region with several instruments that

include fixed FOV and single band or multi bands radiometers. In addition, thermocouples for thermometric measurements, a thermal camera, an emissivity box, a goniometric system and two black bodies (calibration sources) for calibration purposes were used. Details of the instruments are given in Fig.2.

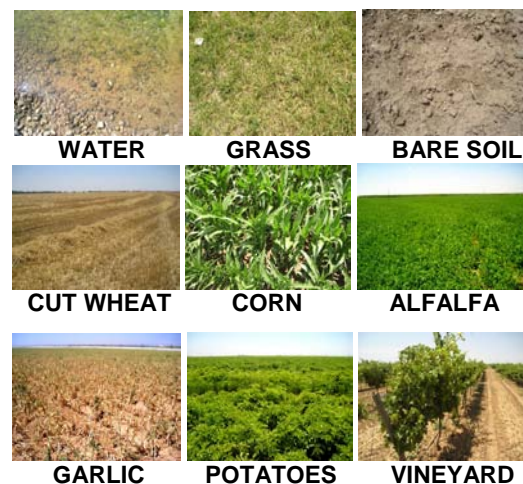


Fig.1. Test parcels analysed during the field campaign.

## 2. MEASUREMENTS PROTOCOL

Prior to the radiometric measurements, a calibration was carried out to compare each instrument with the reference blackbody sources and the thermocouple.

### 2.1 Transects

Transects were taken over several samples surfaces. They were performed concurrently to the satellites and airborne flights over the studied samples. They were carried out taking temperature measurements with field radiometers, at regular steps (3 meters) along a walk performed within a well defined area.

The transects were made half an hour before the scheduled satellite overpasses and ended half an hour later, and we made sure that the sky was clear while taking measurements.

## 2.2 Masts

Thermal measurements were continuously recorded with radiometers located on fixed masts over determined areas (vineyard, bare soil and grass) and periods of time, in coincidence with the airborne/satellite overpasses.

## 2.3 Angular measurements

A study was realized about the angular variation of the infrared brightness temperature of some representative samples at angles between 0° and 60° (at 10° increments). Several series of measurements for each sample were taken. Before and after every series, we measured the sky temperature pointing to the zenith. The two CIMEL radiometers were mounted together and were used simultaneously with the thermal camera to measure radiometric temperature over green grass and bare soil, in the solar and perpendicular plane and at day and night time under different observation angles.

## 2.4 Emissivity measurements: TES method

The emissivity of representative samples was measured by means of the TES (temperature and emissivity separation) method [1] by pointing alternatively to the sample and the zenith using the CIMEL 312-2 radiometer in the Barrax test site.

## 2.5 Emissivity measurements: Box method

The emissivity of representative samples was measured by means of the Box method [2]. The box allows the retrieval of surface emissivity from three different measurements; one with a cold lid (whose emissivity is  $\epsilon=0$ ), another one with a hot lid ( $\epsilon=1$ ), and the last is a measure of the temperature of the hot lid. Three different radiometers were used, namely CIMEL 312-1, EVEREST and RAYTEK MID.

## 2.6 Night campaign

During the night of July, 19<sup>th</sup>, angular and emissivity measurements were carried out over green grass and bare soil.













<p>CIMEL CE 312-1</p>  <p>8-13 <math>\mu\text{m}</math> 8.2-9.2 <math>\mu\text{m}</math> 10.3-11.3 <math>\mu\text{m}</math> 11.5-12.5 <math>\mu\text{m}</math></p> <p>-80 to 60 °C <math>\pm 0.1</math> °C FOV=10°</p>	<p>CIMEL CE 312-2</p>  <p>8-13 <math>\mu\text{m}</math> 11-11.7 <math>\mu\text{m}</math> 10.3-11 <math>\mu\text{m}</math> 8.9-9.3 <math>\mu\text{m}</math> 8.5-8.9 <math>\mu\text{m}</math> 8.1-8.5 <math>\mu\text{m}</math></p> <p>-80 to 60 °C <math>\pm 0.1</math> °C FOV=10°</p>	<p>RAYTEK ST6</p>  <p>8-14 <math>\mu\text{m}</math> -30 to 100 °C <math>\pm 0.5</math> °C FOV: 8°</p>
<p>RAYTEK MID</p>  <p>-40 to 600 °C <math>\pm 0.5</math> °C FOV: 20°</p>	<p>EVEREST 3000.4ZLC</p>  <p>-40 to 100 °C <math>\pm 0.5</math> °C FOV: 4°</p>	<p>THERMOCOUPLE K</p>  <p><math>\pm 0.1</math> °C</p>
<p>Irisys-Iri1001</p> 	<p>EVEREST 1000 calibration source</p>  <p>0 to 60°C <math>\pm 0.3</math>°K</p>	<p>GALAI 204-P calibration source</p>  <p>10 to 100°C <math>\pm 0.2</math>K</p>
<p>EMISSIVITY BOX</p> 	<p>HOT LID</p> 	<p>GONIOMETRIC SYSTEM</p> 

Fig.2. Radiometers and instruments used during the field campaign.

### 3. RESULTS

Different information was retrieved from the ground based measurements. In this section, some results are shown, such as emissivities, angular variation, synergy between SEVIRI and ASTER and synergy between AATSR and CHRIS/PROBA.

#### 3.1 Emissivity measurements: TES method

Fig.3 shows the emissivity results obtained from the *in situ* measurements by applying the TES method.

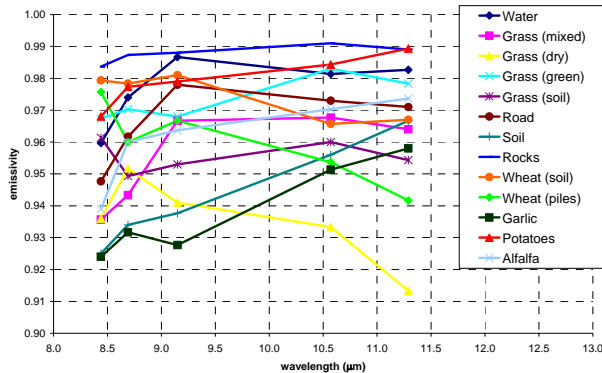


Fig.3. Emissivity values for different samples obtained with the TES method.

#### 3.2 Angular variation

Fig.4 shows the images obtained with the thermal camera when different observation angles are considered. The figure shows the day and night measurements. As it is observed, when there is a significant thermal heterogeneity, it is not possible to study the angular variation of emissivity because the observed spots do not agree in the several angular situations.

The results obtained during the night campaign are shown in Fig. 5, where the angular emissivity values were obtained following the method described in [3] and [4].

#### 3.3 Synergy between SEVIRI and ASTER data

Fig. 6 shows the Normalized Difference Vegetation Index (NDVI) obtained from the Advanced Spaceborne Thermal Emission and Reflection Radiometer (ASTER) image over the region of Barrax on July 15<sup>th</sup> where three intervals are considered. The figure also shows the Spinning Enhanced Visible and Infrared Imager (SEVIRI) pixel size and a region of 5×5 pixels [5].

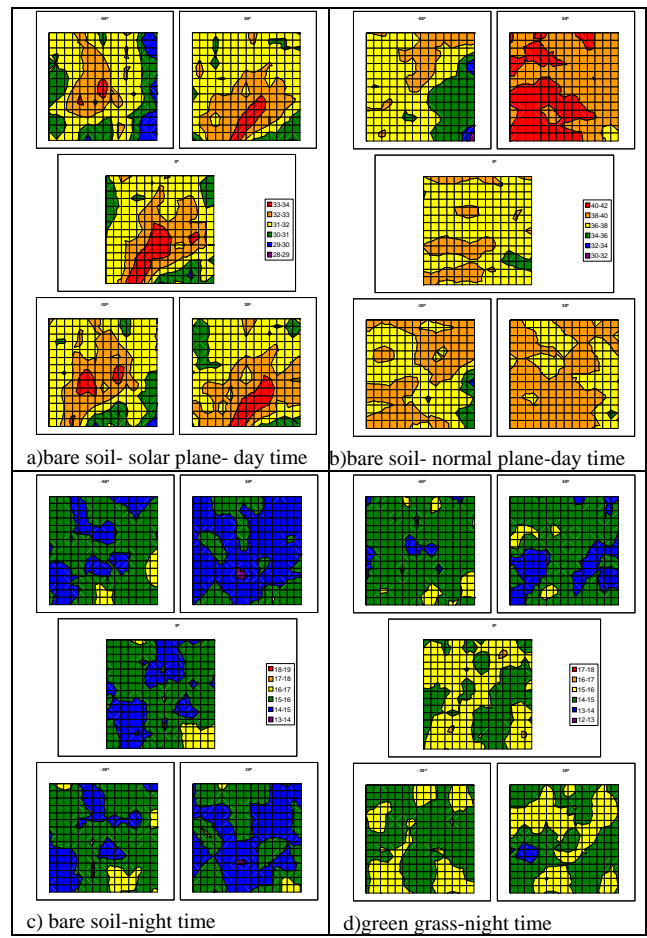
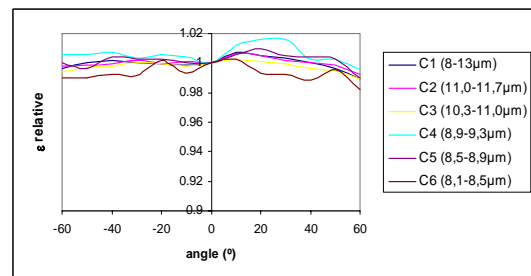
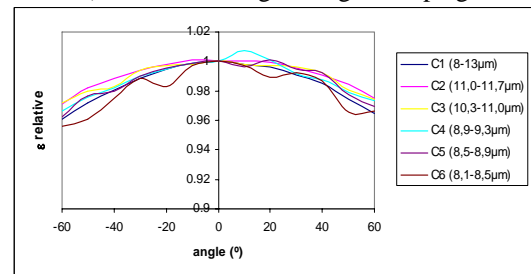


Fig.4. Thermal images of bare soil and green grass under different observation angles.



a) Bare soil during the night campaign



b) Green grass during the night campaign

Fig.5 Angular relative emissivity obtained from the ground measurements at night time for bare soil and green grass samples.

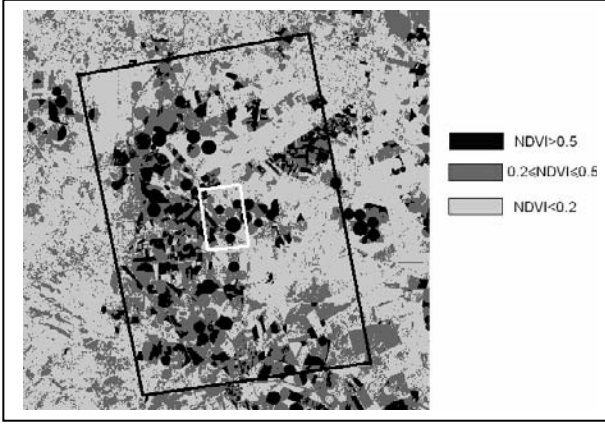


Fig. 6: ASTER NDVI image, SEVIRI pixel size and region of 5×5 SEVIRI pixels.

Firstly, an effective *in situ* temperature was defined according to:

$$T_{\text{eff}} = P_s T_s + P_v T_v + P_m T_m \quad (1)$$

where  $T_s$ ,  $T_v$ , and  $T_m$  are the *in situ* surface temperatures associated to pixels with NDVI values lower than 0.2, higher than 0.5 and between 0.2 and 0.5 respectively.  $P_s$ ,  $P_v$  and  $P_m$  are the corresponding proportions obtained from the ASTER image.

Secondly, these  $T_{\text{eff}}$  were compared with the outputs of the algorithm given by [6]:

$$ST = T_{IR10.8} + [3.17 - 0.64 \cos \theta] \cdot (T_{IR10.8} - T_{IR12.0}) + \left[ -0.05 + \frac{0.157}{\cos \theta} \right] \cdot (T_{IR10.8} - T_{IR12.0})^2 + \left[ 65 - \frac{4}{\cos^2 \theta} \right] \cdot (1 - \varepsilon) + \left[ -11.8 + \frac{5.1}{\cos \theta} \right] \cdot W \cdot (1 - \varepsilon) + \left[ -180 + \frac{24}{\cos \theta} \right] \cdot \Delta \varepsilon + [-4 + 34 \cos \theta] \cdot W \cdot \Delta \varepsilon - 0.6 \quad (2)$$

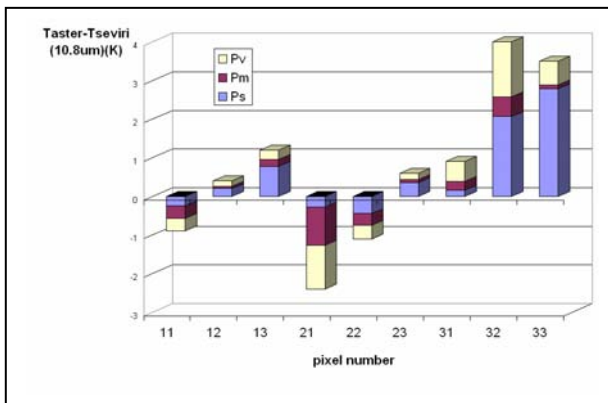


Fig. 7. Difference between ASTER and SEVIRI brightness temperatures in the 10.8μm channels for all pixels in the 3×3 pixel region.

where  $ST$  is the surface temperature (in K),  $T_{IR10.8}$  and  $T_{IR12.0}$  are the at-sensor brightness temperatures of the IR10.8 and IR12.0 SEVIRI thermal channels (in K),  $\varepsilon$  is the mean effective emissivity  $\varepsilon = (\varepsilon_{IR10.8} + \varepsilon_{IR12.0})/2$ ,  $\Delta \varepsilon$  is the emissivity difference  $\Delta \varepsilon = \varepsilon_{IR10.8} - \varepsilon_{IR12.0}$ ,  $W$  is the total atmospheric water vapour ( $\text{g}/\text{cm}^2$ ) and  $\theta$  is the satellite zenith observation angle.

The comparison of the data includes 21 SEVIRI images acquired every 15' between 10:00-15:00 UTC during July, the 15<sup>th</sup> 2004. Effective temperatures were calculated by means of Eq. 1 and were averaged every 15 minutes in order to compare them with LST calculations. The results give rms errors lower than 1.3K when the region of 5×5 pixels is considered. On the other hand, higher errors are obtained when only the central pixel is considered. A single pixel is very susceptible to changes in  $P_s$ ,  $P_m$  and  $P_v$  when changes in latitude and longitude occur.

This fact was also analysed by comparing the radiometric temperatures in the SEVIRI and ASTER channel centered at 10.8μm in a defined region of 3×3 SEVIRI pixels. The difference of this magnitude when the whole region is considered has a value lower than 0.5K. Fig. 7 shows a specific analysis carried out pixel by pixel and includes the information about the proportions of every pixel where the pixel numbers (i,j) correspond to rows and columns respectively.

Comparison of brightness temperatures between SEVIRI and ASTER data shows that the accuracy in latitude and longitude estimation is a critical issue when heterogeneous surfaces are considered and low resolution sensors are used.

### 3.4 Synergy between AATSR and CHRIS data

A set of algorithms based on Split-Window (SW) and Dual-Angle (DA) methods to retrieve land surface temperature (LST) from AATSR data [7] has been evaluated using data from Sparc field campaign.

The evaluation of the algorithms has been made by comparing *in situ* measurements and LST values obtained by applying the algorithms to a Level1b AATSR image acquired on July, 20<sup>th</sup> 2004. The *in situ* measurements correspond to a test area that embraces an extent of 4 by 7 AATSR pixels with a pixel size in the nadir view of 1km by 1km, and 1.5 km by 2km in the forward view.

To evaluate these algorithms in a heterogeneous area, a process of classification has been carried out regarding the different sites that the AATSR pixels are made up of. This allows to analyze statistically the proportions of every of these sites, with their particular values of temperature and emissivity.

With this aim in mind, a CHRIS/PROBA image nearest the transects date has been acquired. This image has a spatial resolution of about 36m, higher than AATSR's. CHRIS operates in 63 spectral bands over the visible/near infrared band. Its images are acquired at along track angles of 55 degrees, 36 degrees and near nadir angles. Thus, for each one of the AATSR pixels studied, it can be overstruck a minimum set of 784 CHRIS pixels (a polygon of about 28 pixels by side).

This high resolution image has been classified through a supervised maximum likelihood classification method, taken 3 different classes as training endmembers, in order to know the proportion of each of the sites in the AATSR pixels. Fig. 8 shows the CHRIS image classified with the 3 endmembers (bare soil in red, green vegetation in green and non-green vegetation in blue) and an overstrike of the area covered by the AATSR pixels.

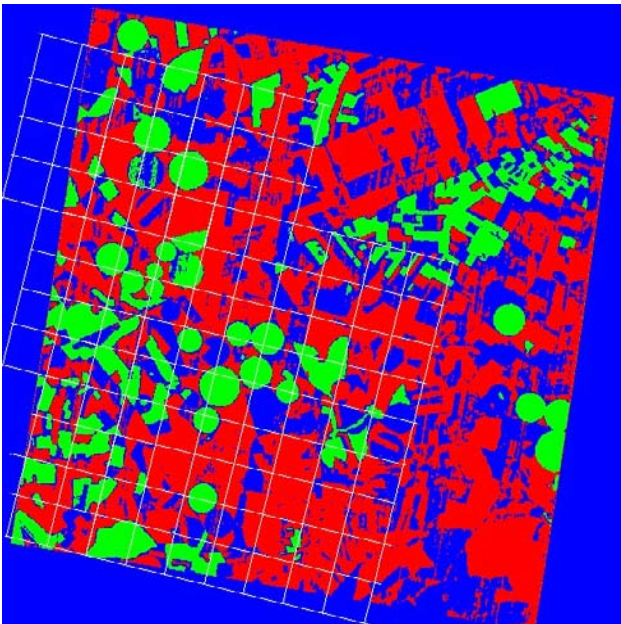


Fig 8. Overstrike of AATSR pixels grid on supervised classification over CHRIS image using 3 endmember classes.

A statistical analysis has been carried out in order to obtain the proportion of the reference areas covered by each AATSR pixel.

The surface temperature of every AATSR pixel has been obtained from all the algorithms proposed. The radiometric temperatures of the AATSR images have been used, as well as the emissivity values of the sites measured for the 11  $\mu\text{m}$  (both nadir and forward views) and 12  $\mu\text{m}$  bands and the amount of total water vapour content of the area.

The results give a Bias lower than 0.6K for all the algorithms considered, and for both single pixels and a

4x4 grid. A higher standard deviation is observed when single pixels are considered, that has been expected to be more sensible to latitud and longitud changes.

The algorithms obtained by DA method incorporate angular effects due to variations of emissivity, water vapour content and radiometric temperature with view angle. Nevertheless, this method supposes that the surface observed at different angles is the same, an assumption that is not always reliable. With the split-window method, pixels from two different bands are used (the ones that have the same area of 1 x 1  $\text{km}^2$ ). In the case of the dual-angle method, information from a pixel of 1 x 1  $\text{km}^2$  with another of 1.5 km x 2.0 km is combined. This way, when AATSR data is processed from Level 0 to Level 1b product, pixels are re-gridded onto a regular grid of a nominal pixel size of 1 x 1  $\text{km}^2$ , so that values of some pixels are allocated according to values of neighbouring pixels.

This effect would be negligible when evaluating DA algorithms in homogeneous surfaces because, in this case, it is not so important to distinguish the value of a pixel from the nearest one. However, in heterogeneous surfaces, like the ones analyzed in the present paper, it is of principal importance to know the area of each pixel; a forward pixel should cover the same area than the nadir pixel, while what occurs is that a forward pixel embrace areas from the neighbouring nadir pixels.

#### 4. CONCLUSIONS

This paper shows the methodology and results obtained from the ground based thermal infrared measurements carried out during the SPARC field campaign. Emissivity and angular variation results were estimated from various samples and observing conditions. Furthermore, a comparison between remote sensed data from SEVIRI, CHRIS, ASTER and AATSR was performed.

#### 5. REFERENCES

1. Gillespie, A., S. Rokugawa, T. Matsunaga, J. S. Cothorn, S. Hook, and A. B. Kahle. A temperature and emissivity separation algorithm for advanced spaceborne thermal emission and reflection radiometer (ASTER) images, *IEEE Transactions on Geoscience and Remote Sensing*, 36, 1113-1126, 1998.
2. Sobrino, J.A. and Caselles, V. A field method for measuring the thermal infrared emissivity, *ISPRS Journal of Photogrammetry and Remote Sensing*, 48:24-31, 1993.
3. Sobrino J.A. and Cuenca, J. Angular variation of thermal infrared emissivity for some natural surfaces from experimental measurements, *Journal of Applied Optics*, 38, No. 18, 3931-3936, 1999.

4. Cuenca J. and Sobrino, J.A. Experimental measurements for studying angular and spectral variation of thermal infrared emissivity. *Applied Optics*, 43, No. 23, 4598-4602. 2004.
5. Gieske, A.S.M, Hendrikse J., Retsios V., Van Leeuwen B., Maathuis B.H.P., Romaguera M., Sobrino, J.A. Timmermans, W.J., Su, Z. (this volume). Processing of msg-1 seviri data in the thermal infrared . Algorithm development with the use of the sparc2004 data set. *ESA/SPARC2004 Proceedings*, 2005.
6. Sobrino, J.A. and Romaguera, M. Land surface temperature retrieval from MSG1-SEVIRI data. *Remote Sensing of Environment*, 92, 247-254, 2004.
7. Sòria, G., Sobrino, J.A., Cuenca, J., Prata, A.J., Jiménez-Muñoz, J.C., Gómez, M. and El-Kharraz, J. Angular effect on Surface Temperature estimation from AATSR data. *IGARSS 2003 – IEEE International Geoscience and Remote Sensing Symposium*. 0-783-7930-6, 2003.